PNAS RESEARCH ARTICLE | ENGINEERING

Carbon-negative cement manufacturing from seawater-derived magnesium feedstocks

Palash Badjatya[a], Abdullah H. Akca[a,b], Daniela V. Fraga Alvarez[c], Baoqi Chang[c], Siwei Ma[a], Xueqi Pang[c], Emily Wang[c], Quinten van Hinsberg[c], Daniel V. Esposito[c,d,e,1], and Shiho Kawashima[a,e,1]

Edited by Werner Sobek, University of Stuttgart; received September 7, 2021; accepted July 12, 2022 by Editorial Board Member Hans J. Schellnhuber

This study describes and demonstrates key steps in a carbon-negative process for manufacturing cement from widely abundant seawater-derived magnesium (Mg) feedstocks. In contrast to conventional Portland cement, which starts with carbon-containing limestone as the source material, the proposed process uses membrane-free electrolyzers to facilitate the conversion of carbon-free magnesium ions (Mg^{2+}) in seawater into magnesium hydroxide [$Mg(OH)_2$] precursors for the production of Mg-based cement. After a low-temperature carbonation curing step converts $Mg(OH)_2$ into magnesium carbonates through reaction with carbon dioxide (CO_2), the resulting Mg-based binders can exhibit compressive strength comparable to that achieved by Portland cement after curing for only 2 days. Although the proposed "cement-from-seawater" process requires similar energy use per ton of cement as existing processes and is not currently suitable for use in conventional reinforced concrete, its potential to achieve a carbon-negative footprint makes it highly attractive to help decarbonize one of the most carbon-intensive industries.

cement | seawater | carbon negative | electrochemistry | magnesium

Portland cement—the key active ingredient in concrete—is one of the most mass-produced materials in the world. Global cement production was 4.1 billion metric tons in 2019 (1) and is projected to grow by 12% by 2050 (2). Unfortunately, the production of Portland cement accounts for ∼7% of global industrial energy consumption and 7 to 8% of anthropogenic CO_2 emissions (2, 3). The main component of Portland cement is calcium oxide (CaO), which is almost exclusively sourced from limestone ($CaCO_3$). As shown in Fig. 1*A*, the conventional manufacturing process starts with excavating and crushing $CaCO_3$, which is sintered with clays in a kiln at temperatures reaching 1,450 °C to produce clinker. This process directly releases CO_2 during calcination of $CaCO_3$ into CaO and indirectly releases CO_2 due to the use of fossil fuels to heat the kiln to high temperatures. The clinker is ground up to produce cement, which is ultimately mixed with aggregates and water to produce concrete.

If society is going to transition to a carbon-neutral or carbon-negative future, which is essential if global warming is to be limited to 1.5 to 2.0 °C (4), alternative construction materials and processing routes must be developed. Currently, the most common approach to reducing the carbon footprint of concrete is to partially replace Portland cement with industrial wastes such as fly ash and slag, although there are challenges associated with quality control and supply of these waste materials as well as practical limits based on scale (5). Geopolymers entirely replace Portland cement with fly ash, slag, and clays and obtain cementing properties through alkali activation (6, 7). $CaCO_3$ calcined clay cements are also derived from $CaCO_3$ but only calcine the clay and use the $CaCO_3$ directly as partial Portland cement replacement, thereby reducing direct and indirect CO_2 emissions (8, 9). Many more alternatives have been proposed and studied (10, 11).

More recently, there has been increasing interest in reducing the carbon footprint of Portland cement by incorporating CO_2 into the final cement material through carbonation of some of the cement phases to produce $CaCO_3$ (12–15). Reactive magnesia (MgO) cement has also been explored as a low-carbon alternative to Portland cements, where solidification occurs via carbonation curing (16, 17). Reports have shown that reactive MgO that undergoes carbon curing in moderately CO_2-rich environments and ambient temperatures produces a hydrated magnesium carbonate-based concrete that can reach compressive strengths of 40 MPa or more (18, 19), which is within the strength range for structural applications. Currently, such reactive MgO cements are most commonly derived from carbon-containing magnesite ($MgCO_3$), which is geographically limited and also requires calcination that directly releases CO_2 (20, 21). Attempts have been made to produce these cements in a carbon-free way from

Significance

The cement industry is one of the largest sources of man-made carbon dioxide (CO_2) emissions and is a hard-to-decarbonize sector that represents a major roadblock to achieving global greenhouse gas emission reduction targets. To address this challenge, the present study demonstrates the key steps in an environmentally friendly process for the manufacture of carbon-negative cement derived from highly abundant magnesium (Mg^{2+}) ions in seawater. If the electricity used to power electrochemical reactors used to harvest Mg^{2+} is derived from carbon-free electricity sources and CO_2 consumed by the process is sourced from the atmosphere or ocean, this carbon-negative process has the potential to transform the world's most carbon-intensive industries into one of its biggest carbon sinks.

Author contributions: X.P., Q.v.H., D.V.E., and S.K. designed research; P.B., A.H.A., D.V.F.A., B.C., S.M., X.P., E.W., and Q.v.H. performed research; P.B., A.H.A., D.V.F.A., B.C., S.M., X.P., E.W., D.V.E., and S.K. analyzed data; and P.B., A.H.A., D.V.F.A., D.V.E., and S.K. wrote the paper.

Competing interest statement: D.V.E. is a co-founder of sHYp, BV PBC.

This article is a PNAS Direct Submission. W.S. is a Guest Editor invited by the Editorial Board.

[1]To whom correspondence may be addressed. Email: de2300@columbia.edu or sk2294@columbia.edu.

This article contains supporting information online at http://www.pnas.org/lookup/suppl/doi:10.1073/pnas.2114680119/-/DCSupplemental.

Published August 16, 2022.

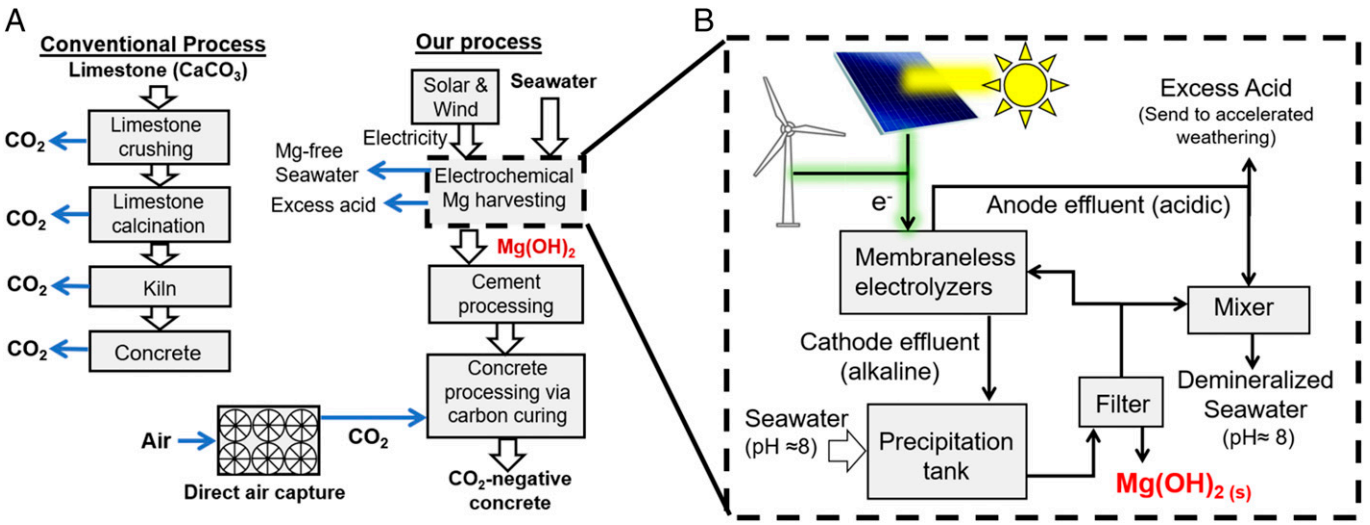

Fig. 1. (*A*) Side-by-side comparison of process flow diagrams for conventional Portland cement and the proposed cement-from-seawater process. (*B*) Process-flow diagram for the electrochemical approach to harvesting alkali earth metal hydroxides from seawater powered by renewable energy.

Mg-silicate feedstocks, which are more abundantly available. As outlined in refs. 22 and 23, Mg-silicates can be subjected to supercritical CO_2 at high temperatures and pressures to first convert them into $MgCO_3$, followed by calcining at ~700 °C to obtain MgO. This was proposed as a potentially net zero-carbon solution due to the inherent carbon-free nature of the silicates and the possibility of recycling the CO_2 within the process flow. However, it has yet to be demonstrably proven with data and life cycle assessment studies to be carbon neutral. Another limitation of Mg cements is their lower alkalinity compared to Portland cements, which precludes their use for reinforced concrete applications that use conventional steel rebar that relies on the high alkalinity of Ca-based Portland cement to prevent corrosion (24). Nonetheless, Mg cements are still well suited for unreinforced components such as concrete masonry units, which currently comprise 15% of all concrete applications (25).

The major challenges for improving the energy efficiency and carbon footprint of concrete manufacturing include sourcing carbon-free or low-carbon raw materials that can be i) produced at low cost and in large quantities, ii) supplied with consistent composition around the world, and iii) used to produce concrete with performance comparable to that of Portland cement-based concrete. Herein, we describe and demonstrate key steps in a CO_2-free process for the production of magnesium-based cement that has the potential to meet all of these requirements. As illustrated in Fig. 1*B*, this process starts by harvesting magnesium from seawater, where dissolved Mg^{2+} represents the fourth most abundant ion in the world's oceans (26). Based on a typical Mg^{2+} concentration of 52 mM, the world's oceans contain enough carbon-free Mg in the form of dissolved Mg^{2+} to supply the world's present-day concrete needs for at least 1 million years. In this study, we extracted Mg^{2+} from seawater by using electrochemical reactors called electrolyzers to temporarily elevate the seawater pH to levels that cause Mg^{2+} to react with hydroxyls and form insoluble magnesium hydroxide ($Mg(OH)_2$) particles that can be easily separated from seawater. In addition to producing the alkaline stream used to form $Mg(OH)_2$, the electrolyzer also produces dilute, salty hydrochloric acid (HCl). A portion of the acidic stream is used to neutralize the demineralized seawater before it is returned to the ocean, but the process also produces excess HCl. If produced at high enough purity, the HCl may be sold on the open market or used as part of "accelerated weathering" schemes that involve neutralization with alkaline basalt or olivine mineral formations (27–29). Importantly, the process shown in Fig. 1*B* returns pH-neutral water back to the ocean and can be carried out without any CO_2 emissions if the electricity used to power electrolysis is generated by renewable solar and wind.

The idea of extracting alkaline earth metals from seawater or brine solutions using electrochemical processing was previously explored by Gilliam et al. (30), who developed electrochemical cells based on anion exchange membranes (AEMs) and cation exchange membranes (CEMs) to generate alkaline salt solutions that were combined with a CO_2 source to produce solid carbonate minerals. Ellis et al. (31) also used electrolysis for cement processing when they used three-compartment membrane-based electrolyzers to aid in the breakdown of $CaCO_3$ as a part of processing for conventional Portland cement. However, this process is still only carbon neutral at best due to the use of $CaCO_3$ as the starting material. In contrast to previous efforts, the proposed process in Fig. 1*B* starts with carbon-free Mg^{2+} ions and harvests it in the form of solid $Mg(OH)_2$. $Mg(OH)_2$ is a versatile precursor material that can be converted into a viable construction material by multiple pathways. First, $Mg(OH)_2$ can be converted to reactive MgO and utilized as cement similar to $MgCO_3$-derived MgO (32, 33). This process requires lower calcination temperatures (500 to 1,000 °C) (32, 34) than Portland cement and does not involve direct CO_2 emissions from the source material. This high temperature calcination step may be avoided by exposing compacted $Mg(OH)_2$ powder to CO_2 under elevated pressure. De Silva et al. (35) subjected $Mg(OH)_2$ compacts to 20 atm of CO_2 and measured compressive strengths exceeding 60 MPa after 6 hours of carbonation curing. However, that study did not consider the source of the $Mg(OH)_2$.

Herein, we report proof-of-principle experiments based on three key steps that are central to the cement-from-seawater process illustrated in Fig. 1: i) electrochemical generation of salty NaOH and HCl using membraneless electrolyzers, ii) precipitation of $Mg(OH)_2$ from seawater, and iii) a low-temperature carbonation process for direct conversion of $Mg(OH)_2$ into magnesium carbonate-based binder. After the properties and performance of the Mg-based binder are characterized, the energy use and carbon footprint of the overall process are compared to conventional Portland and Mg cements. Finally, opportunities and

challenges for implementing the proposed process at scale are discussed. Throughout this article, all precursor $Mg(OH)_2$ powders are referred to as "cement," while conventional cement is referred to as "Portland cement" and the matrix of solids obtained after carbonation is referred to as "binder." Seawater-derived precipitated $Mg(OH)_2$ is compared against commercial $Mg(OH)_2$, with the latter referred to as "standard" brucite.

Results and Discussion

Electrochemical Production of Acid and Base with Membraneless Electrolyzers. Going back to at least 1865, it has been known that Mg^{2+} ions can be harvested from seawater by elevating the pH of seawater such that Mg^{2+} reacts with hydroxyls (OH^-) to form insoluble $Mg(OH)_2$ (26). $Mg(OH)_2$ is still commercially obtained by this means through the addition of alkaline quick lime (CaO) to seawater (26). However, the production of CaO, such as for Portland cement, has a large carbon footprint because it is obtained from $CaCO_3$. In contrast, our process uses a membraneless electrolyzer (Fig. 2*A*) to generate salty base and acid directly from seawater according to Eqs. **1** and **2**, respectively:

$$\textbf{Oxidation half reaction}: H_2 \rightarrow 2H^+ + 2e^- \qquad [1]$$
$$\mathrm{E} = -0.059 \cdot (\mathrm{pH_a})\ \mathrm{V\ vs.\ NHE},$$

$$\textbf{Reduction half reaction}: 2H_2O + 2e^- \rightarrow H_2 + 2OH^- \qquad [2]$$
$$\mathrm{E} = -0.059 \cdot (\mathrm{pH_c})\ \mathrm{V\ vs.\ NHE},$$

where E is the reversible cell potential and pH_a and pH_c are the pH at the anode and cathode, respectively. The expressions for E assume a standard temperature of 298 K and standard state partial pressure of H_2 of 1 bar. During operation, H_2 from the cathode can be directly transferred to the anode where it is oxidized, or it can be collected from the cathode effluent and recycled back to the feed stream (*SI Appendix*, Fig. S1). In either case, Fig. 2*A* shows how electrolyte is pumped through two porous electrodes to sweep the salty acid and salty base into separate effluent streams, resulting in the following overall reaction:

$$\textbf{Overall reaction}: H_2O \rightarrow H^+|_{anode} + OH^-|_{cathode} \Delta\mathrm{E} = 0.059 \cdot \Delta\mathrm{pH}, \qquad [3]$$

where ΔE is the minimum voltage required to drive the overall reaction at the desired pH difference $\Delta pH = pH_c - pH_a$. Talabi et al. (36) previously demonstrated a similar concept using membraneless electrolyzers for producing acid and base from pH-neutral sodium sulfate and potassium nitrate solutions but did so through water electrolysis that involved the oxygen evolution reaction at the anode. However, the reaction scheme given by Eqs. **1**–**3** is better for generating acid and base in seawater because i) the hydrogen oxidation reaction is far more favorable than the undesirable chlorine evolution reaction, ii) the required cell voltage is substantially lower than that required for water electrolysis, and iii) it avoids safety concerns about mixing O_2 and H_2 because O_2 is not generated at the anode.

The electrolyzer concept in Fig. 2*A* was demonstrated using platinized porous carbon foam electrodes. Fig. 2*B* shows scanning electron microscopy (SEM) images of one such electrode, where the microporous structure of the carbon foam and discrete platinum nanoparticles can be seen in the low- and high-magnification images, respectively. Two identical porous Pt/C electrodes were positioned parallel to each other within a

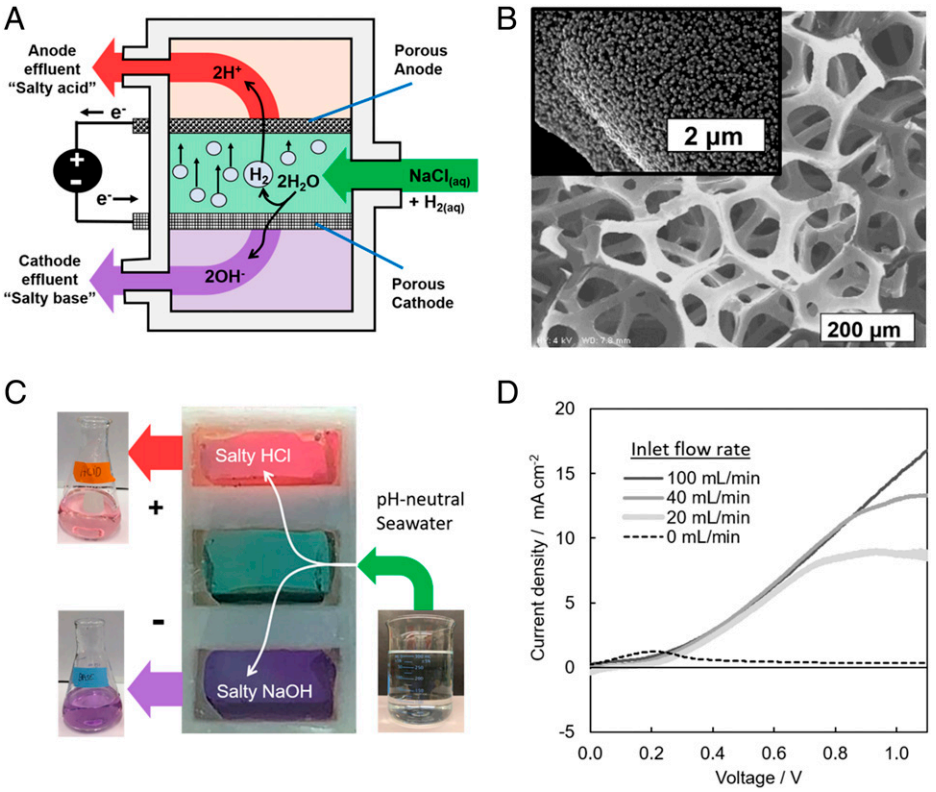

Fig. 2. (*A*) Schematic of membraneless electrolyzer used for splitting seawater into acidic and alkaline streams. (*B*) SEM images of as-made platinized carbon foam electrodes. (*C*) Photograph of membraneless electrolyzer during steady-state electrolysis of natural seawater in the presence of a pH indicator dye, which turns purple or red in alkaline and acidic environments, respectively. (*D*) *i-V* curves recorded for membraneless electrolyzer recorded in H_2-saturated Mg-free natural seawater at several different inlet volumetric flow rates. Also shown is an *i-V* curve taken in the absence of flowing electrolyte or dissolved H_2.

three-dimensional(3D)-printed membraneless electrolyzer that was outfitted with windows to allow for in situ imaging. A photograph of the device during operation in Mg-free natural seawater is provided in Fig. 2*C*, where H_2-saturated natural seawater was fed into the right side of the device at 0.33 mL s^{-1} and salty acid and salty base effluent streams left the upper left and lower left ports, respectively. For this experiment, universal pH indicator dye was added to the inlet stream, causing it to change color based on the local pH. The pH-neutral feed stream is pale green, while the alkaline cathode effluent stream turns purple and the acidic anode effluent stream turns red. The absence of purple or red plumes within the electrode gap indicates that there was limited cross-over of the liquid phase products. This observation is further supported by measurement of the pH of the anode (pH_a = 3.38) and cathode (pH_c = 10.03) effluent streams, which are similar to those expected for the chosen operating conditions (pH_a = 3.19 and pH_c = 10.82).

The two-electrode current-voltage (*i-V*) characteristics of the electrolyzer were also recorded and are provided in Fig. 2*D* for different inlet volumetric flow rates. In the absence of any $H_{2(aq)}$ in the inlet stream, the electrolyzer generates no significant current across the voltage range analyzed. Running the same measurement in H_2-saturated Mg-free seawater resulted in *i-V* curves with onset voltages of around 0.2 V, followed by linear increases in current density up until the point where mass transfer of dissolved H_2 to the anode limited the overall reaction and resulted in a limiting current plateau at high voltages. This was confirmed by increasing the volumetric flow rate of the H_2-saturated inlet stream, which resulted in a monotonic increase in limiting current with flow rate (*SI Appendix*, Fig. S2). The relatively shallow slope of the *i-V* curves can be largely attributed to concentration overpotentials caused by the buildup of a pH differential between the two electrodes. In contrast, overpotential losses were substantially reduced when the electrolyzer was operated in 0.5 M H_2SO_4 (*SI Appendix*, Fig. S2) because no significant pH changes occurred.

Although the membraneless electrolyzer generates a relatively dilute salty base stream, its alkalinity is still sufficient to drive Mg^{2+} precipitation and can be increased further through optimization of the electrode and device designs. It should also be noted that salty HCl and salty NaOH can also be generated using electrodialysis stacks based on bipolar membranes composed of CEMs and AEMs (37–39). Gilliam et al. (30) similarly employed electrochemical cells containing separated CEMs and AEMs to generate alkaline and acidic streams from brine solutions based on the reactions given in Eqs. **1**–**3**. However, the ion exchange membranes in these electrodialysis-type devices present significant technoeconomic challenges with respect to both cost and lifetime (40). In general, the lack of stable AEMs that can operate in seawater is a major impediment to direct seawater electrolysis technologies (41). Thus, an electrolyzer that completely avoids the need for membranes has an inherent advantage for operation in seawater. The electrodes of an electrolyzer can also be prone to fouling or degradation, but the recirculating scheme of Fig. 1*B* ensures that raw seawater is first sterilized in the alkaline precipitation tank before reaching the membraneless electrolyzer. Removal of Mg^{2+} ions before the seawater reaches the electrolyzer has the added benefit of avoiding $Mg(OH)_2$ deposits from forming on the cathode, another common concern in seawater electrolysis (42, 43).

Precipitation and Harvesting of $Mg(OH)_2$ from Seawater. As described above, Mg^{2+} ions may be converted into solid $Mg(OH)_2$ by reaction with OH^-:

$$Mg^{2+} + 2OH^- \rightarrow Mg(OH)_{2(s)} \quad K_{sp}^{\circ} = 5.61 \times 10^{-12}\ M^3, \quad [4]$$

where K_{sp}° is the solubility product constant at 25 °C (44). Consistent with Le Chatelier's principle, increasing pH shifts equilibrium to the right, causing Mg^{2+} to be converted into insoluble $Mg(OH)_2$ particles. The $Mg(OH)_{2(s)}$ initially forms a colloidal suspension that gives the solution a milky color (Fig. 3*A*, *Insets*), but further growth of particles leads to precipitation as gravity forces larger particles downward. As shown in *SI Appendix*, Fig. S3, Mg^{2+} should begin precipitating from 25 °C seawater at pH ≈9.1, and 95% of Mg^{2+} should precipitate at pH ≈9.7.

To determine how much OH^- is required to precipitate Mg^{2+} from seawater with a target yield, varying amounts of NaOH were added to 350-mL aliquots of natural seawater. Following centrifugation and rinsing steps detailed in *Materials and Methods*, the collected $Mg(OH)_{2(s)}$ was dried overnight and weighed. The composition of several samples was also evaluated using thermogravimetric analysis (TGA), allowing for determination of the mass of harvested $Mg(OH)_2$ by subtracting the weight of residual water and small quantities of $CaCO_3$ from the total weight of the sample. Fig. 3*A* shows how the

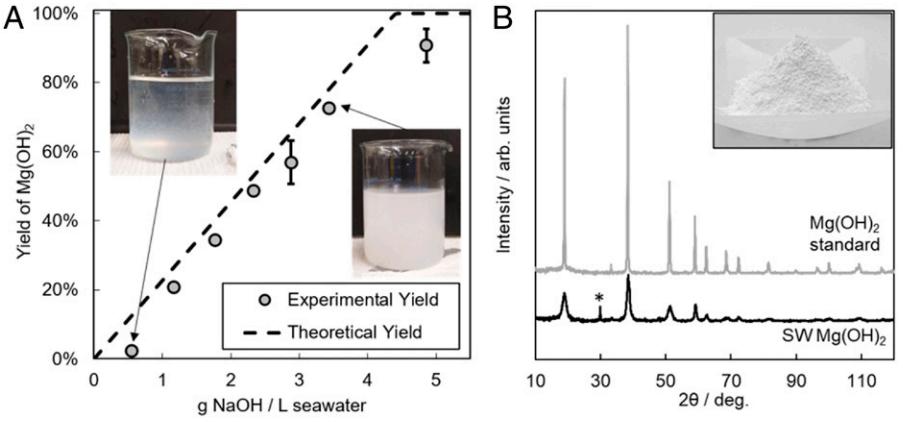

Fig. 3. Precipitation of Mg^{2+} from seawater. (*A*) Theoretical and experimental yields of $Mg(OH)_2$ obtained from precipitation of natural seawater titrated with NaOH as a function of the amount of NaOH titrant. Insets show photos of natural seawater titrated with two different amounts of NaOH. Theoretical yield was calculated based on the solubility constant product for $Mg(OH)_2$ at room temperature (Eq. 4) and neglecting any buffering effects from sulfate or carbonate. (*B*) XRD patterns for standard brucite $Mg(OH)_2$ and seawater-derived (SW) $Mg(OH)_2$ were obtained by precipitation using 4.86 g NaOH per liter of seawater and rinsing with deionized water. All XRD peaks were associated with $Mg(OH)_2$, except for the peak marked with *, which is attributed to $CaCO_3$. Inset shows a photograph of seawater-derived $Mg(OH)_2$ after pulverization. arb., arbitrary; deg., degree.

amount of added NaOH affected the yield of harvested $Mg(OH)_{2(s)}$, defined as the fraction of Mg^{2+} ions in the natural seawater sample that are collected in the form of $Mg(OH)_{2(s)}$. For this calculation, the concentration of Mg^{2+} initially present in the sample was determined to be 50 mM based on the amount of $Mg(OH)_2$ collected after titrating the seawater sample with excess NaOH (4.86 g NaOH per liter of seawater); 50 mM is similar to the "typical" concentration of Mg^{2+} in the world's oceans, 52.8 mM (45). Fig. 3*A* shows that the yield increased linearly with the amount of NaOH added to seawater up until ≈4 g NaOH per liter of seawater, at which point over 2 moles of NaOH had been added per mole Mg^{2+} present in the seawater. For constant titrant dosing of 4.86 g NaOH per liter, yields of 90.7 ± 4.8% were obtained for small-scale experiments producing 0.94 g $Mg(OH)_2$, while yields increased to 99.9 ± 6.3% for a larger 62.4-g batch of $Mg(OH)_2$ due to lower $Mg(OH)_2$ loss during transfer from the centrifuge bottle to the drying rack. For all titrations, Fig. 3*A* shows that the experimentally determined yields are in excellent agreement with the theoretical yield. Samples with varying number of freshwater rinse cycles were also characterized by TGA, showing that a single rinse cycle was sufficient to remove NaCl below the detection limit (*SI Appendix*, Fig. S4). Although it is highly desirable to minimize the amount of freshwater used in a scaled-up version of this process, especially in water-stressed locations, all additional experiments were carried out using two or three rinse cycles so as to minimize the role of residual NaCl on strength performance of the Mg cements.

After drying in air, the $Mg(OH)_2$ filter cake was first crushed into a fine white powder (Fig. 3*B*, *Inset*) and passed through sieves to give particle sizes between 0.4 μm and 75 μm that were comparable to the standard brucite powder (*SI Appendix*, Fig. S5). SEM images of the dried and pulverized seawater-derived $Mg(OH)_2$ revealed a rough surface morphology without a well-defined shape, in contrast to the standard brucite particles that contained visible prismatic crystallites (*SI Appendix*, Fig. S6). X-ray diffraction (XRD) results (Fig. 3*B*) show that both standard brucite and seawater-derived samples had prominent brucite peaks (PDF #44–1482), although the latter also contained a small peak around $2\theta = 29.5°$ that can be assigned to calcite ($CaCO_3$, PDF #05–0586) (46). Derivative TGA weight loss curves for seawater-derived $Mg(OH)_2$ after two rinse cycles (*SI Appendix*, Fig. S7) confirmed the presence of calcite (10 mass %) in addition to residual amounts of water (3.5 mass %).

Carbonation Curing of $Mg(OH)_2$ Mixtures. Before undergoing carbonation curing, distilled water, a coreactant, was added to the dried $Mg(OH)_2$ powders to maintain a water to solids mass ratio of 0.3. Wet powders made from both standard brucite and seawater-derived $Mg(OH)_2$ were then compacted into cylindrical samples and cured inside a sealed incubator where the samples were exposed to a humidified CO_2 environment (20% CO_2 concentration by volume at 85% relative humidity) at 1 bar total pressure for 48 h. Detailed results of curing the standard brucite for varying amounts of time and varying water to solids ratios are reported in ref. 47, but only the 48-h and 0.3 water to solids ratio results are included here. To compare the microstructure of the binders made from the two different source materials, the compacts were crushed back into a powder form and characterized by TGA, XRD, and SEM (Fig. 4). Derivative weight loss TGA curves (Fig. 4 *A* and *B*) show that both types of samples still exhibited peaks at ≈400 °C associated with residual (i.e., unreacted) brucite, but they also reveal the emergence of new peaks at low temperature (≈25 to 250 °C) attributed to a combination of free or physically bound water and water removed from Mg carbonate hydrate phases, such as hydromagnesite ($4MgCO_3.Mg(OH)_2.4H_2O$), dypingite ($4MgCO_3.Mg(OH)_2.5H_2O$), and nesquehonite ($MgCO_3.3H_2O$). Additional mass change signal is also seen at higher temperatures (≈400 to 500 °C), which can be attributed to further mass loss from the Mg carbonate phases (48–50), although TGA is not able to distinguish between them.

The presence of carbonates in both types of cured specimens was also confirmed by XRD, as seen in the diffractograms for samples cured for 48 h in Fig. 4 *C* and *D*. For the cured standard brucite sample, significant decreases in the intensities of the brucite peaks were accompanied by the emergence of features that can be ascribed to the hydromagnesite and nesquehonite carbonate phases. Using the Rietveld refinement method (*SI Appendix*, Section XIV), the mass percentages of hydromagnesite, brucite, and nesquehonite were estimated to be 52.2%, 40.0%, and 7.8%, respectively. The detailed compositions for all samples are provided in *SI Appendix*, Table S1. In contrast to the XRD patterns for the cured standard brucite samples, those for the cured seawater-derived $Mg(OH)_2$ samples (Fig. 4*D*) showed that nesquehonite is the predominant carbonate phase. The composition (mass %) for the seawater-derived sample was calculated to be 49.3% nesquehonite, 42.9% residual brucite, 5.9% calcite, and 1.9% hydromagnesite (*SI Appendix*, Table S1). Nesquehonite has also been observed in CO_2-cured $Mg(OH)_2$ compacts studied by De Silva et al. (35). Consistent with previous studies carrying out carbonation of Mg precursors at low pressure and temperature (19, 35, 51), none of the diffraction patterns in Fig. 4 *C* and *D* contain peaks associated with $MgCO_3$, which is only known to form at higher temperature and pressure (52, 53). It is important to note that the carbonate compositions presented here are effectively average values from the entire specimen. Due to the role of CO_2 transport limitations on the carbonation process, the extent of carbonation is always expected to be greatest in the outer shell of the specimen compared to the core, with these differences being greatest during the earliest stages of the carbonation curing process. This was confirmed by using energy-dispersive X-ray spectroscopy to measure normalized carbon concentration profiles of cross-sections of cylindrical specimens at curing times of 3 h, 2 d, and 5 d (*SI Appendix*, Fig. S13). These results show that the outer shell of the specimen is converted to carbonate phases to much greater extent than the inner core after 3 h, with clear differences still present after 2 d of curing time. After 5 d of carbonation curing, the carbon content of the inner core is within 20% of the outer surface. More in-depth investigation of the permeability of these specimens should shed more light on the progression of carbonation and help to guide the development of optimal processing conditions for structures of varying size.

Clear evidence of carbonate formation was also observed in SEM images of both types of samples (Fig. 4 *E* and *F*). For the cured standard samples, rosette-like features are seen that are characteristic of hydromagnesite, as observed in other reactive Mg-based systems (54). If present throughout the microstructure, such features can serve to both densify and cement the material system and subsequently form a binder phase, similar to the effect of calcium-silicate-hydrate in Portland cement systems (24). In contrast, SEM images of the cured seawater-derived sample reveal needle-like features that are characteristic of nesquehonite (32, 54, 55). Dypingite also exhibits rosette-like features (17, 56) and is characterized by a similar XRD pattern as hydromagnesite, but hydromagnesite proved a better fit

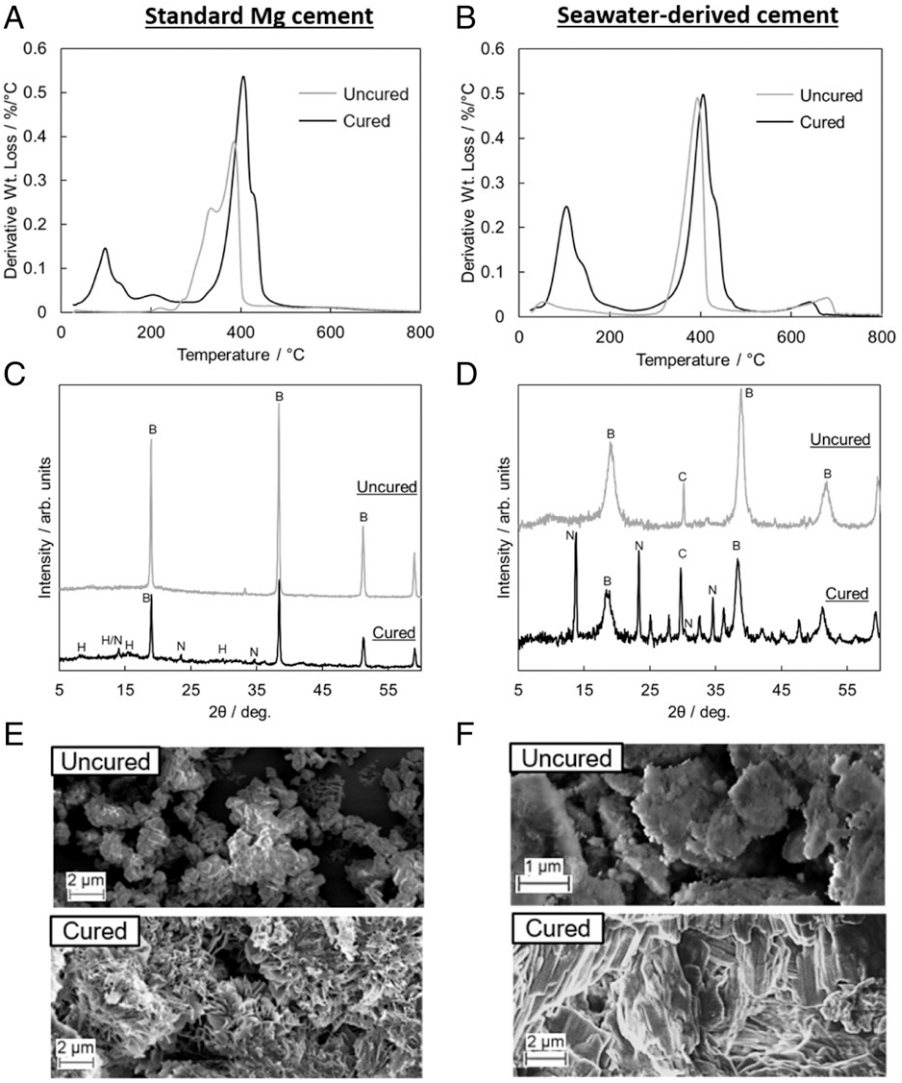

Fig. 4. Microstructural characterization of standard (left column) and seawater-derived (right column) Mg cement samples before and after carbonation curing. (*A*–*F*) Both samples were created using a water to solids mass ratio of 0.3 and were cured for 48 h in humidified CO_2 at 20% concentration and 1 bar total pressure. Samples were characterized before and after curing using (*A* and *B*) TGA, (*C* and *D*) XRD, and (*E* and *F*) SEM. The following phases were identified in the diffractograms of *C* and *D*: B, brucite; H, hydromagnesite; N, nesquehonite; C, calcite. Comparison data for the standard brucite samples are provided from ref. 47. arb., arbitrary; deg., degree; Wt, weight.

for the data than dypingite based on quantitative analysis of XRD and TGA results. Nevertheless, given the similar chemical composition and morphology of hydromagnesite and dypingite, their impact on composite strength and durability is expected to be comparable. The moles of CO_2 absorbed per mole of Mg precursor during formation of either carbonate are also the same, meaning that incorrect identification of hydromagnesite versus dypingite does not affect interpretation of the carbon uptake by the composite.

Several factors related to the $Mg(OH)_2$ source material might explain the differences in composition of the cured standard and seawater-derived binders, including differences in $Mg(OH)_2$ particle shape, particle and agglomerate size distributions, surface roughness, and trace impurities. Even with the same curing conditions and identical mix design, the attributes of the source material can lead to the formation of different polymorphs due to the influence of their starting structure and composition on local reaction conditions within the material during curing. For example, differences in the density and size of agglomerated particles in the source material can be expected to alter the local concentrations of CO_2 and H_2O within the agglomerates, with higher densities and larger agglomerate sizes resulting in lower concentrations of reactant species within the interior of the agglomerates (57). Since reaction rate expressions for different reaction pathways can have different reaction orders with respect to reactants (52, 53), it stands to reason that relative changes in local concentrations of H_2O and CO_2 within a specimen can lead to different products. However, other possible explanations, including interactions with impurity calcite crystallites and/or the formation of CO_2-rich bubbles within nanoscopic voids within the particles (57), cannot be ruled out at this time.

Additional standard Mg cement samples were prepared and cured to study change in the degree of carbonation for curing times between 3 h and 120 h. The carbonate composition was analyzed quantitatively using TGA and XRD and is presented in *SI Appendix*, Section XIV. The results show that the amount of carbonates continued to increase beyond 48 h, while the amount of residual brucite decreased further. It can be reasonably expected that the seawater-derived cement will similarly show continued carbon uptake with increased curing time since a similar amount of unreacted brucite remained available after 48 h.

Mechanical Performance of Mg-Binders. To view the impact of carbonation on the strength of the resulting binders, compressive strength tests were carried out on standard brucite and seawater-derived cylinders subjected to carbonation curing for 48 h. While the standard brucite samples resulted in a compressive strength of 33.4 ± 2.0 MPa, the compressive strength of seawater-derived Mg binder samples was found to be 22.5 ± 1.9 MPa, which is ≈33% lower than that of the standard samples.

Interestingly, both the standard brucite and seawater-derived samples had very similar initial densities (1.49 g/cm^3 and 1.44 g/cm^3, respectively) and final densities (1.69 g/cm^3 and 1.63 g/cm^3, respectively), suggesting that factors other than density may also be affecting compressive strength. For example, differences in particle size (*SI Appendix*, Fig. S5) and/or agglomerate size distributions may affect packing behavior during compaction and therefore alter the permeability of H_2O or CO_2 through the source material during carbonation. Particle size distribution and morphology may also affect the surface area available for products to form. It should also be recalled that the seawater-derived brucite contained ≈10% $CaCO_3$ by mass; this $CaCO_3$ can be expected to be inert during CO_2 curing, such that it is effectively reducing the "active" $Mg(OH)_2$ portion of the cement, which could lead to lower strength. Differences in the amounts of residual (unconverted) $Mg(OH)_2$ could also affect strength, although the mass % residual $Mg(OH)_2$ was within 3% for both types of samples (*SI Appendix*, Table S1). Lastly, CO_2 curing leads to the formation of carbonate phases with different morphologies in the two cured brucite systems, which may also impact the strength of the binding matrix. Further investigations into all of these factors will be required to understand how the microstructure and composition of seawater-derived and standard brucite samples impact strength gain at multiple stages of the curing process.

Despite differences in 48-h strength, seawater-derived cement can be expected to continue to gain strength with additional curing time, as we recently reported for standard brucite (47). Moreover, conversion to nesquehonite is preferable from a carbon sequestration standpoint as the formation of this phase involves the absorption of more CO_2 per unit weight of precursor cement than conversion to hydromagnesite. Equally important, the seawater-derived binder's strength of 22.5 MPa is still comparable to the early compressive strength (<7 d after mixing) of ordinary Portland cement concrete and suitable to meet building codes (24, 58).

Energy Use and Carbon Footprint. Table 1 contains a comparison of the expected energy use and carbon footprint of the proposed seawater-derived Mg cement manufacturing process to conventional $CaCO_3$-based Portland cement and $MgCO_3$-derived Mg cement processes. The functional unit is 1 ton of material (cement/concrete), and for Mg cement concretes, complete conversion of Mg precursors to carbonate (nesquehonite) is assumed as an upper limit on the amount of CO_2 absorbed by these concretes. Methods and further assumptions underlying the calculations used to generate this table, along with the data sources, can be found in *SI Appendix*, Section XV.

Focusing first on energy use, Table 1 shows that the Mg concretes consumed more energy than Portland cement concrete. MgO-derived concrete used the most energy, which resulted from the energy-intensive mining and processing steps associated with the $MgCO_3$ precursor, as well as the energy required to source CO_2 for the carbonation process from direct air capture. Cement produced by the proposed seawater-derived Mg process had a lower energy demand and required less CO_2 per unit weight than MgO-derived cement, but it had a higher energy requirement than Portland cement.

Despite requiring more energy than Portland cement concrete, the proposed cement-from-seawater process is still highly attractive because almost all of the energy inputs can be provided in the form of low- or zero-carbon electricity generated from renewable sources. Table 1 shows that the seawater-derived concrete can be carbon-negative, which is possible because this process is powered by electricity, starts with carbon-free feedstock materials, and consumes CO_2 during the carbon curing process (up to 755 kg CO_2 per ton of $Mg(OH)_2$ for 100% conversion to nesquehonite). Meanwhile, conventional $CaCO_3$- and $MgCO_3$-based cements have large carbon footprints due to direct and indirect CO_2 emissions associated with calcination processes, which also lead to high carbon footprints for the resultant concretes. The carbon emissions of both conventional processes can be lowered if renewable energy is used for electricity-dependent processes, but electricity only typically comprises 5 to 10% of the total energy requirements (59, 60). There has also been substantial interest in capturing CO_2 released from $MgCO_3$ or $CaCO_3$ during the calcination process and reabsorbing that same CO_2 for the formation of the Mg concrete or emerging carbonate-based Portland cement concretes (13, 31, 61). However, these methods can never be carbon-negative because the maximum amount of CO_2 that can be reabsorbed by the system is less than the amount released during production due to the carbonate feedstock. As noted in the introduction, an alternative route using MgO obtained from silicates could also provide a carbon-negative concrete by using a similar carbonation procedure as for seawater-derived Mg cement concrete. However, due to lack of data in the literature and absence of any environmental product

Table 1. Comparison of energy use and CO_2 emissions of cement and concrete production among conventional Portland cement derived from $CaCO_3$, MgO cement derived from $MgCO_3$, and the proposed $Mg(OH)_2$ cement derived from seawater

	Cement manufacturing		Concrete manufacturing	
Mineral feedstock	Energy use (kJ/ton of cement)	CO_2 emissions (kg/ton of cement)	Energy use (kJ/ton of concrete)	CO_2 emissions (kg/ton of concrete)
Portland cement from $CaCO_3$	3.8×10^6	793	8.8×10^5	150
MgO from $MgCO_3$	5.9×10^6	1,850	4.3×10^6	323
$Mg(OH)_2$ from seawater	4.4×10^6	0*	2.8×10^6	−93*

*The CO_2 footprint for production of seawater-derived Mg cement assumes that all electricity used to power $Mg(OH)_2$ harvesting and processing is provided exclusively by a carbon-free electricity generator. If current US grid electricity is used to power the process, the carbon footprints for seawater-derived Mg cement and concrete are 550 and 61 kg/ton, respectively.

All other details of the calculations and key assumptions are included in *SI Appendix*, Tables S3–S8.

declarations of the former product, that approach was excluded from the comparison here.

Conclusions and Future Prospects. This study has demonstrated the viability of a process for producing Mg-based cement from seawater-derived feedstock materials that has the potential to turn one of the world's most carbon-intensive industries into one of its biggest carbon sinks. However, significant advances must be made for this carbon-negative cement manufacturing scheme to become reality. First, it is essential that low-cost renewable electricity be used to power the process. As recently as 2019, only 20.1% of electricity in the United States was derived from renewables and 18.9% was derived from low-carbon nuclear power (62). Based on the current carbon intensity of US grid electricity (0.45 kg CO_2 kWh^{-1}), the estimated carbon footprint of the proposed process would be +61 kg CO_2 per ton of concrete, which represents a reduction of 67% compared to conventional Portland cement, but this is not carbon-negative. Moving forward, carbon-negative cement involving electrochemical processing will only be possible if there is aggressive adoption of low-carbon electricity generators. Secondly, it is important to note that Mg-based cement is not suitable for use in steel reinforced concretes because its lower alkalinity compared to Portland cement provides less protection against corrosion of iron-based rebar (63). To overcome this, alternatives such as fiber-reinforced polymer composites, which do not corrode at low alkalinity, can be used as internal or external reinforcement (64, 65). While such reinforcement alternatives are being explored, unreinforced components such as masonry, paver, or sidewalk blocks can be early applications for facilitating adoption of this material. Another challenge to widespread adoption of Mg cements is achieving sufficient carbonation of thicker elements used in larger structures, which becomes an issue due to the longer carbonation times required for CO_2 to diffuse into their interior. Further research is needed to study the same; however, until then, smaller/thinner elements such as blocks/panels can be developed, which can then be assembled together, for example, using external reinforcement to create larger elements such as walls and columns. Moreover, investigations involving the durability of this material, both long-term and at different temperatures, are imperative. Finally, we note that a manufacturing plant based on our process should ideally be located on the coast in close proximity to the ocean. While this presents an opportunity for coastal communities, which comprise a significant fraction of the Earth's population (66), additional energy and carbon penalties would be incurred to transport precast seawater-derived concrete or vast volumes of seawater inland.

Materials and Methods

Chemicals. Except for natural seawater (Nutri-Seawater, Nature's Ocean), all solutions were prepared using 18.2 MΩ-cm deionized water. Solutions were prepared using concentrated sulfuric acid (Certified ACS plus, Thermo Fisher Scientific), sodium chloride (ACS Reagent grade, Sigma-Aldrich), sodium hydroxide (Certified ACS, Thermo Fisher Scientific), HCl (Certified ACS plus, Thermo Fisher Scientific), potassium tetrachloroplatinate (99.99% trace metal basis, Sigma-Aldrich), and universal pH indicator dye (pH 4 to 10, Sigma-Aldrich). Anhydrous $Mg(OH)_2$ (Reagent grade, 95%, Sigma-Aldrich) was used as the source material for control samples. Mg-free natural seawater was prepared by first adding 4.86 g of NaOH per liter of seawater to precipitate Mg^{2+} as $Mg(OH)_2$. The solution was centrifuged at 5,000 rpm for 1 h and decanted before the pH was lowered back to pH ≈7.50 by titration with 1 M HCl. The electrolytes were purged with either nitrogen gas (N_2, Purity Plus 99.999% purity) or hydrogen gas (H_2, Purity Plus 99.999% purity).

Electrode Fabrication. Electrode supports were made from carbon foam (McMaster-Carr, 100 pores per inch), sheet resistance = 7.87×10^{-2} ohms/sq) with titanium foil used as an electrical connection and feedthrough. Each electrode was cut into a 15 mm × 33 mm piece, with the thickness of the electrode inserted into the electrolysis cell cut to a thickness of 3.2 mm (*SI Appendix*, Fig. S8). Before electrodeposition, the carbon foam underwent a two-step chronoamperometry procedure for 10 s total in 0.5 M H_2SO_4, whereby the potential was alternated between 0.4 V versus Ag|AgCl and −0.8 V versus Ag|AgCl with pulse widths of 5 s. Electrodes were platinized by carrying out cyclic voltammetry (CV) at 100 mV s^{-1} in a 3 mM K_2PtCl_4 + 0.5 M NaCl electrolyte (pH = 2.60) for 21 cycles between −0.7 V versus Ag|AgCl and +0.3 V versus Ag|AgCl.

Electrolyzer Fabrication. Electrolyzers were 3D printed using natural color acrylonitrile butadiene styrene using a MakerGear M3-ID 3D printer (Makerbot Industries). The cell walls were printed with 100% solid infill. Electrodes were inserted into slits in the cell body and sealed using epoxy (ClearWeld J.B Weld). Glass microscope slides serving as windows for in situ imaging were also attached with epoxy. High-density polyethylene connectors (1/8″ ID, Cole-Parmer) were epoxied to the inlet and outlet ports.

Electrolysis Experiments. All electrochemical experiments were carried out using a Biologic SP-300 bipotentiostat. A schematic of the setup used for most electrolysis experiments is provided in *SI Appendix*, Fig. S9. Electrolyzer inlet and outlet ports were connected to feed reservoir and effluent collection beakers, respectively, using silicone tubing (Masterflex L/S, Cole Parmer). The effluent tubes were fed through peristaltic pumps (NE-9004, Syringe Pump), which were set to identical volumetric flow rates to ensure equal volumetric flow rates through the anode and cathode. The feed reservoir was constantly purged with H_2 gas (99.999% purity) at 1 atm. The series resistance of the cell was measured by electrochemical impedance spectroscopy. Before electrolysis, electrodes were characterized by conducting CV cycling at 20 mV s^{-1} for 10 cycles in deaerated 0.5 M H_2SO_4 (*SI Appendix*, Fig. S10). Next, the cell was filled with synthetic or Mg-free natural seawater, and electrodes were subjected to five more CV cycles while sweeping voltage between −0.2 V and 1.1 V at 20 mV s^{-1}. The pH of the anodic and cathodic effluent streams was measured under steady-state operation while applying a cell voltage of 1.0 V.

Precipitation Experiments. Mg^{2+} was precipitated from natural seawater at room temperature by adding diluted NaOH at concentrations ranging from 0.03 to 0.5 M to an Erlenmeyer flask containing 175 to 700 mL of seawater. After NaOH was added, the solution was allowed to equilibrate for 5 min before being transferred into a 500-mL Nalgene bottle for centrifugation. Each sample underwent two or three rinsing steps, and each centrifugation step was carried out at 5,000 rpm using an Avanti J-E Series JLA-10.500 Beckman Coulter Centrifuge. When the sample underwent two rinsing steps, the first centrifugation step lasted 2 min, the second step lasted 5 min, and the final step lasted 15 min. When the sample underwent three rinsing steps, the first centrifugation step lasted 2 min, the second and third steps lasted 5 min, and the final step lasted 15 min. After each centrifugation step except for the final one, the supernatant was decanted and replaced by 400 mL deionized water, and the bottle was shaken by hand for ≈2 min. Following the final centrifugation step, $Mg(OH)_{2(s)}$ was collected from the bottle, spread onto a horizontally suspended cloth, and dried overnight in a fume hood using a fan.

Powder Processing. Standard Sigma-Aldrich $Mg(OH)_2$ powder was used as obtained. Dry seawater-derived $Mg(OH)_{2(s)}$ was ground using a ceramic mortar and pestle for 1 min, then pulverized in a ball milling device (SPEX 8000 Mixer/Mill) for 5 min (*SI Appendix*, Fig. S11). Subsequent sieving using 53-μm and 75-μm sieve sizes resulted in $Mg(OH)_2$ powder with a particle size distribution similar to that of the standard brucite (*SI Appendix*, Fig. S5). Particle size distributions were determined using a laser-based particle sizer (Beckman Coulter, Inc., LS 13 320 MW).

Sample Compaction and Curing. *SI Appendix*, Fig. S12 shows the steps involved with compacting and curing the $Mg(OH)_2$. Briefly, 40 g of dry $Mg(OH)_2$ powder was combined with distilled water at a water to solids mass ratio of 0.3. The wet powder was then divided into three identical cylindrical specimen molds, each with a diameter of 1 inch and a height of 1 inch. Each specimen

was compacted in two layers, where each layer was subjected to a compaction pressure of 3 MPa for 2 min using an MTS Criterion C43 Electromechanical Testing Machine. The water to solids ratio and the compaction pressure were selected based on a recent study by our groups that systematically explored the influence of processing conditions on the compressive strength of binders made by accelerated carbonation of laboratory-grade brucite (47). After compaction, specimens were demolded and weighed and immediately placed in an incubator, which maintained an environment of 20 vol. % CO_2, with a 25 °C ± 1 °C operation temperature and 80% ± 5% relative humidity. The compacts (three repeat samples) were subjected to 48 h of curing. After removal from the incubator, the cured specimens were weighed and their dimensions were measured.

Compressive Strength Measurement. Specimens were capped with high-strength gypsum paste, which was applied to each end of the specimen and solidified against a smooth surface. This capping ensured that each specimen had orthogonal and smooth bearing surfaces in order to minimize stress concentrations and maintain loading uniformity during the compression test. The compression tests were conducted using a hydraulic testing machine (Instron 5984 Universal Testing Machine) at a displacement rate of 0.15 mm/min.

Characterization. Characterization was performed on both raw and cured samples to help identify effects of carbonation. The raw powder was used as is for characterization. For the cured samples, one specimen from each batch was picked and pulverized into a fine powder. It was then characterized by TGA, XRD, and SEM. About 15 mg of powder was used for the TGA scans in a TA Instruments Q50 thermogravimetric analyzer. The samples were heated from room temperature to 1,000 °C at a rate of 20 °C min^{-1} in an inert N_2 atmosphere. XRD characterization was performed using a Malvern Panalytical XPert^3 powder diffractometer. Powdered samples were packed into a circular sample holder and exposed to Cu Kα radiation (operating conditions: 40 V and 40 mA). XRD scans were carried out for 2θ angles between 5° and 80° at a step size of 0.04° and step interval of 0.05 s per step. MDI's JADE 6 software was used for phase identification, and Maud software was used to apply the Rietveld refinement method. Further details of phase composition calculations, based on both XRD and TGA results, are provided in *SI Appendix*, Section III. SEM images were obtained using a Zeiss Sigma VP Scanning Electron Microscope. Powder was scattered on carbon tape and coated with Au Pd to reduce charging.

Data, Materials, and Software Availability. All study data are included in the article and/or *SI Appendix*. Design files for the membraneless electrolyzer are freely available at echem.io

ACKNOWLEDGMENTS. S.K. and D.V.E. acknowledge seed funding from the Columbia University School of Applied Sciences and Engineering Interdisciplinary Research Seed program. A.H.A. acknowledges financial support from The Scientific and Technical Research Council of Turkey (TÜBİTAK). We acknowledge Scott Banta for use of his laboratory's centrifuge, Alissa Park for helpful discussions and the use of equipment in her laboratory, and Athanasios Bourtsalas for helpful discussions.

Author affiliations: [a]Department of Civil Engineering and Engineering Mechanics, Columbia University, New York, NY 10027; [b]Department of Civil Engineering, Yıldız Technical University, Esenler, 34220 İstanbul, Turkey; [c]Department of Chemical Engineering, Columbia University, New York, NY 10027; [d]Columbia Electrochemical Energy Center, Columbia University, New York, NY 10027; and [e]Lenfest Center for Sustainable Energy, Columbia University, New York, NY 10027

1. US Geological Survey, *Mineral Commodity Summaries 2020* (*Mineral Commodity Summaries*, US Geological Survey, Reston, VA, 2020), p. 204.
2. International Energy Agency, Technology Roadmap–Low-Carbon Transition in the Cement Industry. (2018).
3. R. M. Andrew, Global CO_2 emissions from cement production, 1928-2018. *Earth Syst. Sci. Data* **11**, 1675–1710 (2019).
4. Intergovenmental Panel on Climate Change, "Summary for policymakers" in *Global Warming of 1.5°C: An IPCC Special Report on the Impacts of Global Warming of 1.5°C Above Pre-Industrial Levels and Related Global Greenhouse Gas Emission Pathways, in the Context of Strengthening the Global Response to the Threat of Climate Change, Sustainable Development, and Efforts to Eradicate Poverty*, V. Masson-Delmotte *et al.*, Eds. (Intergovenmental Panel on Climate Change, 2018, pp. 3–26).
5. K. L. Scrivener, V. M. John, E. M. Gartner, Eco-efficient cements: Potential economically viable solutions for a low-CO_2 cement-based materials industry. *Cement Concr. Res.* **114**, 2–26 (2018).
6. Alkali Activated Materials: State-of-the-Art Report, RILEM TC 224-AAM, J. Provis, J. Deventer, Eds. (Springer Netherlands, ed. 1, 2014), pp. XIV, 388.
7. J. L. Provis, Alkali-activated materials. *Cement Concr. Res.* **114**, 40–48 (2018).
8. Y. Dhandapani, T. Sakthivel, M. Santhanam, R. Gettu, R. G. Pillai, Mechanical properties and durability performance of concretes with limestone calcined clay cement (LC3). *Cement Concr. Res.* **107**, 136–151 (2018).
9. H. Justnes, T. A. Østnor, *Alternative Binders Based on Lime and Calcined Clay* (Springer Netherlands, Dordrecht, 2015), pp. 51–57.
10. M. C. G. Juenger, F. Winnefeld, J. L. Provis, J. H. Ideker, Advances in alternative cementitious binders. *Cement Concr. Res.* **41**, 1232–1243 (2011).
11. C. J. Shi, A. F. Jimenez, A. Palomo, New cements for the 21st century: The pursuit of an alternative to Portland cement. *Cement Concr. Res.* **41**, 750–763 (2011).
12. K. Vance *et al.*, Direct carbonation of $Ca(OH)_2$ using liquid and supercritical CO_2: Implications for carbon-neutral cementation. *Ind. Eng. Chem. Res.* **54**, 8908–8918 (2015).
13. Q. H. Li *et al.*, A novel strategy for carbon capture and sequestration by rHLPD processing. *Front. Energy Res.* **4**, 10.3389/fenrg.2015.00053 (2016).
14. Z. Li, Z. He, X. Chen, The performance of carbonation-cured concrete. *Materials (Basel)* **12**, 3729 (2019).
15. J. Kline, C. Kline, "CO_2 capture from cement manufacture and reuse in concrete" in *IEEE Industry Applications Magazine* (IEEE, 2020), pp. 42–49.
16. A. Al-Tabbaa, "Reactive magnesia cement" in *Eco-Efficient Concrete*, F. PachecoTorgal, S. Jalali, J. Labrincha, V. M. John, Eds. (Woodhead Publishing, 2013), pp. 523–543.
17. C. Unluer, "Carbon dioxide sequestration in magnesium-based binders" in *Carbon Dioxide Sequestration in Cementitious Construction Materials*, F. Pacheco-Torgal, C. Shi, A. P. Sanchez, Eds. (Woodhead Publishing, 2018), chap. 7.
18. N. T. Dung, C. Unluer, Sequestration of CO_2 in reactive MgO cement-based mixes with enhanced hydration mechanisms. *Constr. Build. Mater.* **143**, 71–82 (2017).
19. N. T. Dung, C. Unluer, Development of MgO concrete with enhanced hydration and carbonation mechanisms. *Cement Concr. Res.* **103**, 160–169 (2018).
20. W. G. Shen *et al.*, Is magnesia cement low carbon? Life cycle carbon footprint comparing with Portland cement. *J. Clean. Prod.* **131**, 20–27 (2016).
21. S. A. Walling, J. L. Provis, Magnesia-based cements: A journey of 150 years, and cements for the future? *Chem. Rev.* **116**, 4170–4204 (2016).
22. E. Gartner, H. Hirao, A review of alternative approaches to the reduction of CO_2 emissions associated with the manufacture of the binder phase in concrete. *Cement Concr. Res.* **78**, 126–142 (2015).
23. E. M. Gartner, D. E. Macphee, A physico-chemical basis for novel cementitious binders. *Cement Concr. Res.* **41**, 736–749 (2011).
24. S. Mindess, J. F. Young, D. Darwin, *Concrete* (Prentice Hall, Upper Saddle River, NJ, 2003).
25. E. National Academies of Sciences, *Medicine, Gaseous Carbon Waste Streams Utilization: Status and Research Needs* (The National Academies Press, Washington, DC, 2019), pp. 256.
26. M. Seeger, W. Otto, W. Flick, F. Bickelhaupt, O. S. Akkerman, "Magnesium compounds" in *Ullmann's Encyclopedia of Industrial Chemistry* (Wiley-VCH Verlag GmbH & Co. KGaA, 2011) 10. 1002/14356007.a15_595.pub2.
27. K. Z. House, C. H. House, D. P. Schrag, M. J. Aziz, Electrochemical acceleration of chemical weathering as an energetically feasible approach to mitigating anthropogenic climate change. *Environ. Sci. Technol.* **41**, 8464–8470 (2007).
28. G. H. Rau, J. R. Baird, Negative-CO_2-emissions ocean thermal energy conversion. *Renew. Sustain. Energy Rev.* **95**, 265–272 (2018).
29. G. H. Rau, H. D. Willauer, Z. J. Ren, The global potential for converting renewable electricity to negative-CO_2-emissions hydrogen. *Nat. Clim. Change* **8**, 621 (2018).
30. R. J. Gilliam *et al.*, Low voltage electrochemical process for direct carbon dioxide sequestration. *J. Electrochem. Soc.* **159**, B627–B628 (2012).
31. L. D. Ellis, A. F. Badel, M. L. Chiang, R. J. Y. Park, Y. M. Chiang, Toward electrochemical synthesis of cement–An electrolyzer-based process for decarbonating $CaCO_3$ while producing useful gas streams. *Proc. Natl. Acad. Sci. U.S.A.* **117**, 12584–12591 (2020).
32. S. Ma, A. H. Akca, D. Esposito, S. Kawashima, Influence of aqueous carbonate species on hydration and carbonation of reactive MgO cement. *J. CO_2 Util.* **41**, 101260 (2020).
33. S. Ruan, E.-H. Yang, C. Unluer, Production of reactive magnesia from desalination reject brine and its use as a binder. J. CO_2 Util. **44**, 101383 (2020).
34. H. Dong, E.-H. Yang, C. Unluer, F. Jin, A. Al-Tabbaa, Investigation of the properties of MgO recovered from reject brine obtained from desalination plants. *J. Clean. Prod.* **196**, 100–108 (2018).
35. P. De Silva, L. Bucea, V. Sirivivatnanon, Chemical, microstructural and strength development of calcium and magnesium carbonate binders. *Cement Concr. Res.* **39**, 460–465 (2009).
36. O. O. Talabi, A. E. Dorfi, G. D. O'Neil, D. V. Esposito, Membraneless electrolyzers for the simultaneous production of acid and base. *Chem. Commun. (Camb.)* **53**, 8006–8009 (2017).
37. B. D. Patterson *et al.*, Renewable CO_2 recycling and synthetic fuel production in a marine environment. *Proc. Natl. Acad. Sci. U.S.A.* **116**, 12212–12219 (2019).
38. I. A. Digdaya *et al.*, A direct coupled electrochemical system for capture and conversion of CO_2 from oceanwater. *Nat. Commun.* **11**, 4412 (2020).
39. M. D. Eisaman *et al.*, CO_2 extraction from seawater using bipolar membrane electrodialysis. *Energy Environ. Sci.* **5**, 7346–7352 (2012).
40. F. Sabatino *et al.*, Evaluation of a direct air capture process combining wet scrubbing and bipolar membrane electrodialysis. *Ind. Eng. Chem. Res.* **59**, 7007–7020 (2020).
41. S. Dresp, F. Dionigi, M. Klingenhof, P. Strasser, Direct electrolytic splitting of seawater: Opportunities and challenges. *ACS Energy Lett.* **4**, 933–942 (2019).
42. X. Y. Lu *et al.*, A sea-change: Manganese doped nickel/nickel oxide electrocatalysts for hydrogen generation from seawater. *Energy Environ. Sci.* **11**, 1898–1910 (2018).
43. W. M. Tong *et al.*, Electrolysis of low-grade and saline surface water. *Nat. Energy* **5**, 367–377 (2020).
44. J. R., Rumble, "Solubility product constants of inorganic salts", in CRC Handbook of Chemistry and Physics, (CRC Press/Taylor & Francis, Boca Raton, FL, Internet Version 2020), Edition 101.
45. M. P. Hain, D. M. Sigman, J. A. Higgins, G. H. Haug, The effects of secular calcium and magnesium concentration changes on the thermodynamics of seawater acid/base chemistry: Implications for Eocene and Cretaceous ocean carbon chemistry and buffering. *Global Biogeochem. Cycles* **29**, 517–533 (2015).

46. J. Dweck, P. M. Buchler, A. C. V. Coelho, F. K. Cartledge, Hydration of a Portland cement blended with calcium carbonate. *Thermochim. Acta* **346**, 105–113 (2000).
47. A. H. Akca, S. Ma, D. Esposito, S. Kawashima, Evaluation of mechanical performance of compacted magnesium hydroxide after carbonation curing. *J. Mater. Civ. Eng.* **34**, 04022056 (2022).
48. R. L. Frost, S. Bahfenne, J. Graham, W. N. Martens, Thermal stability of artinite, dypingite and brugnatellite–Implications for the geosequestration of green house gases. *Thermochim. Acta* **475**, 39–43 (2008).
49. G. Jauffret, J. Morrison, F. P. Glasser, On the thermal decomposition of nesquehonite. *J. Therm. Anal. Calorim.* **122**, 601–609 (2015).
50. V. Vágvölgyi *et al.*, Controlled rate thermal analysis of hydromagnesite. *J. Therm. Anal. Calorim.* **92**, 893–897 (2008).
51. A. Botha, C. A. Strydom, Preparation of a magnesium hydroxy carbonate from magnesium hydroxide. *Hydrometallurgy* **62**, 175–183 (2001).
52. J. Highfield, J. Chen, M. Haghighatlari, J. Åbacka, R. Zevenhoven, Low-temperature gas–solid carbonation of magnesia and magnesium hydroxide promoted by non-immersive contact with water. *RSC Advances* **6**, 89655–89664 (2016).
53. W. B. White, Thermodynamic equilibrium, kinetics, activation barriers, and reaction mechanisms for chemical reactions in Karst Terrains. *Environmental Geology* **30**, 46–58 (1997).
54. N. T. Dung, A. Lesimple, R. Hay, K. Celik, C. Unluer, Formation of carbonate phases and their effect on the performance of reactive MgO cement formulations. *Cement Concr. Res.* **125**, 105894 (2019).
55. V. Ferrini, C. De Vito, S. Mignardi, Synthesis of nesquehonite by reaction of gaseous CO_2 with Mg chloride solution: Its potential role in the sequestration of carbon dioxide. *J. Hazard. Mater.* **168**, 832–837 (2009).
56. I. M. Power, S. A. Wilson, J. M. Thom, G. M. Dipple, G. Southam, Biologically induced mineralization of dypingite by cyanobacteria from an alkaline wetland near Atlin, British Columbia, Canada. *Geochem. Trans.* **8**, 13 (2007).
57. S. F. Jones, G. M. Evans, K. P. Galvin, Bubble nucleation from gas cavities–A review. *Adv. Colloid Interface Sci.* **80**, 27–50 (1999).
58. American Concrete Institute Committee 318, *Building Code Requirements for Structural Concrete (ACI 318-08) and Commentary* (American Concrete Institute, 2008).
59. E. Worrell, K. Kermeli, C. Galitsky, *Energy Efficiency Improvement and Cost Saving Opportunities for Cement Making: An ENERGY STAR Guide for Energy and Plant Managers* (US Environmental Protection Agency, 2013).
60. F. Schorcht, I. Kourti, B. Scalet, S. Roudier, L. Delgado Sancho; Joint Research Centre of the European Commission, *Best Available Techniques (BAT) Reference Document for the Production of Cement, Lime and Magnesium Oxide: Industrial Emissions Directive 2010/75/EU* (*JRC Reference Reports*, Publications Office of the European Union, Luxembourg, 2013).
61. M. M. Bomgardner, "Curing cement's CO_2 weakness" in *Chemical & Engineering News* (American Chemical Society, 2014), pp. 15–16.
62. Monthly Energy Review, Department of Energy (U.S. Energy Information Administration). https://www.eia.gov/totalenergy/data/monthly/archive/00352202.pdf. (2022).
63. S. Ahmad, Reinforcement corrosion in concrete structures, its monitoring and service life prediction—A review. *Cement Concr. Compos.* **25**, 459–471 (2003).
64. M. Z. Naser, R. A. Hawileh, J. A. Abdalla, Fiber-reinforced polymer composites in strengthening reinforced concrete structures: A critical review. *Eng. Struct.* **198**, 109542 (2019).
65. C. E. Bakis *et al.*, Fiber-reinforced polymer composites for construction–State-of-the-art review. *J. Compos. Constr.* **6**, 73–87 (2002).
66. United Nations, "Factsheet: People and Oceans" in *The Ocean Conference* (New York), pp.1–7.